The impact of imposed Couette flow on the stability of pressure-driven flows over porous surfaces

Article *in* Journal of Engineering Mathematics · February 2022

DOI: 10.1007/s10665-021-10195-3

3 authors, including:

Harunori Yoshikawa
Université Côte d'Azur
51 PUBLICATIONS **373** CITATIONS
SEE PROFILE

Parisa Mirbod
University of Illinois at Chicago
47 PUBLICATIONS **224** CITATIONS
SEE PROFILE

J Eng Math: (2022) 132:15
https://doi.org/10.1007/s10665-021-10195-3

The impact of imposed Couette flow on the stability of pressure-driven flows over porous surfaces

Saman Hooshyar · Harunori N. Yoshikawa · Parisa Mirbod

Received: 10 July 2021 / Accepted: 12 November 2021

Abstract We present linear stability analysis of a pressure-driven flow in a fluid-layer overlaying porous media in the presence of a Couette component introduced by an upper impermeable wall. We model the flow dynamics in the porous media by the Brinkman equation and couple it with the Navier–Stokes equation for flows in the fluid-layer. The effect of the Couette flow component on flow stability is discussed in detail with varying the permeability and the relative thickness of the fluid to porous layers. The results show that the effect changes from destabilizing to stabilizing at a certain velocity of the upper wall. This velocity, called the cutoff velocity, is highly dependent on the porous medium characteristics. The cutoff velocity drops as the permeability of the porous surface decreases or the fluid layer thickness increases. Imposing a Couette flow shifts the instability mode from fluid mode to porous mode due to generation of vortices at the interface when the porous layer approaches an impermeable wall. We also performed energy budget analysis to provide a physical interpretation for the behavior of the flow. We found that the energy production due to the Reynolds stress causes the disturbances to grow which consequently triggers the instability.

Keywords Darcy–Brinkman equation · Linear instability · Plane Poiseuille–Couette flow · Porous media

1 Introduction

Studying hydrodynamic stability of flows facilitates determining when and how the laminar flow breaks down and its transition to turbulence occurs. The stability analysis of viscous flows over a permeable surface has been studied extensively in recent years due to their wide range of applications. An example of industrial application is infiltration process in liquid composite molding (LCM), where the resin impregnates dry fibers can be considered as flow over porous media. LCM is widely used in high quality production of advanced composites such as turbine blades, airplane wings, and bridge deck sub components [1]. Other examples are recovery of oil trapped in geological porous media [2], catalytic reactors and heat exchangers [3], and cooling electrical components and metallic sponges

S. Hooshyar · P. Mirbod (✉)
Department of Mechanical and Industrial Engineering, University of Illinois at Chicago, 842 W. Taylor Street, Chicago, IL 60607, USA
e-mail: pmirbod@uic.edu

H. N. Yoshikawa
Université Côte d'Azur, CNRS UMR 7010, Institut de Physique de Nice, 06100 Nice, France

Published online: 31 December 2021

[4]. In this study, we focus on the effects of a Couette flow component on the stability of a pressure driven Poiseuille flow (PF) over a porous medium as a method of flow control. While the effects of a porous surface or a superposed Couette flow component on the stability of Poiseuille flow have been analyzed individually, little attention has been paid to this industrially relevant flow configuration except for a recent work by Samanta [5].

Chang et al. [6] were the first who examined the stability of plane Poiseuille flow (PF) in a fluid overlying a porous layer. They adopted Darcy's law as the governing equation in the porous-layer and employed an interface condition proposed by Beavers and Joseph [7]. They found that depending on the values of depth ratio L/H defined as the ratio of fluid layer thickness L to porous layer thickness H, Darcy number $\sqrt{\kappa}/H$ defined as the ratio of the square root of permeability κ to the porous layer thickness, and Beavers–Joseph constant value the neutral stability curves might be bi-modal or tri-modal. Later, Hill and Straughan [8] studied a similar problem to Chang et al. [6], but they added a Brinkman porous transition layer on top of the Darcy-type porous material to eliminate the discontinuity in velocity profile between the fluid and porous layers. It is shown that neutral curves have bi-modal shapes and are significantly affected by the depth ratio and the Brinkman transition layer depth. Later, Liu et al. [9] also studied the stability of PF in a fluid–porous channel flow and used the Brinkman's model for the flow dynamics in a porous medium. They compared the obtained results with those of the other models and reported significant differences between them. Tilton and Cortelezzi [10] performed linear stability analysis to investigate the destabilizing effects of wall permeability. They coupled the Navier–Stokes and the Volume-Averaged Navier–Stokes equations to characterize the behavior of the flow inside the fluid-layer and the porous-layer, respectively. They also assumed a small permeability to neglect the inertial effects in the flow dynamics in the porous layer and concluded that the stability of Poiseuille flow in a channel decreases as the permeability of porous surface increases. Recently, Wu and Mirbod [11] examined the effects of the depth ratio, permeability, and porosity on the stability of PF by solving the coupled Navier–Stokes and Brinkman equations. They showed that the stability depends both on $\alpha = H/\sqrt{\kappa}$, called *permeability parameter*, and $\delta = L/H$ but only through its product $\gamma = \alpha\delta$. Presence of walls with velocity slip (e.g., porous walls) plays a major role in the stability of stratified flows [12–14]. Chattopadhyay et al. [15], performed linear stability analysis of a pressure-driven flow of immiscible two-fluids of stratified viscosity and density through a channel with a bottom anisotropic and inhomogeneous porous wall. Their detailed parametric study revealed that the instability features are influenced by the presence of porous wall, the non-zero velocity perturbations at the liquid–porous interface, and perturbations at liquid–liquid interface arising due to stratification in viscosity.

To the best of our knowledge, Potter [16] pioneered the linear stability analysis of Poiseuille–Couette flow (PCF) of a Newtonian fluid through a smooth channel. He investigated the stability of a two-dimensional PCF between two infinite smooth parallel plates by finding the asymptotic solution of the corresponding Orr–Sommerfeld equation. He found that, in general, superposing the Couette flow on a Poiseuille flow imposes a stabilizing effect except for a small range where the non-dimensional upper wall velocity W lies within 0.2 to 0.4 of the maximum Poiseuille flow velocity U. He also showed that the flow is stable to infinitesimal disturbances for all Reynolds numbers when $W > 0.7U$. Reynolds and Potter [17] employed the formal expansion method to analyze instability of parallel shear flows subjected to infinitesimal and finite disturbances. Their result reveals that PCF is always stable to infinitesimal disturbances when the Couette components exceeds approximately 53% of the bulk average velocity but remains unstable to finite disturbances. In 1967, Hains [18] carried out a numerical determination of the stability of plane PCF and compared his results with Thomas [19] and Potter [16]. He found that the Couette flow component stabilizes the modes associated with the Poiseuille flow. His results showed that the critical Reynolds number approaches infinity as the wall speed increases in either upstream or downstream direction [20]. The linear stability of a plane PCF in the presence of a cross-flow, i.e. injection of fluid through a wall, was also addressed by Guha and Frigaard [21] where they used the energy analysis to interpret the instability. At small cross-flow Reynolds number R_{inj}, the critical layers shift and the energy production decreases gradually. However, the flow destabilizes and then stabilizes at small and large R_{inj}, respectively. This stabilization appears to be due to a decrease in the rate of energy transfer from base flow to disturbances.

To the best of the authors' knowledge, Chang et al. [22] was the first who studied the linear stability of plane PCF in a fluid overlying a porous medium. They showed that at small depth ratio $\hat{d}$ the Couette flow destabilizes the Poiseuille flow and induces the tri-modal shape of neutral curve. However, at depth ratio $\delta > 0.4$, the Cou-

ette flow exerts stabilizing effects on the system. Unlike Darcy's model where the viscosity in the porous layer is neglected, the Brinkman model introduces effective viscosity to describe the friction caused by macroscopic shear [9]. Employing Brinkman equation eliminates the need to apply complicated boundary conditions at the fluid–porous interface since the velocity and pressure fields are continuous throughout the channel domain. Samanta [5] coupled the Navier–Stokes and Brinkman equation instead of Darcy's law to capture the momentum diffusion effect at the fluid–porous interface. His results show that the presence of Couette flow intensifies the most unstable fluid layer mode while it attenuates the most unstable porous layer mode. Furthermore, the energy budget analysis reveals that the energy transfer from base flow to disturbances via Reynolds stress triggers the flow instability. In this study, we also employ Brinkman and Navier–Stokes equations to characterize the flow behavior in the channel; however, we follow the work by Hill and Straughan [8] to impose continuity of tangential stress at the fluid–porous interface instead of jump tangential stress proposed by Beavers and Joseph [7].

The novelty of this work is (1) we performed an extensive study on the effects of permeability parameter α and depth ratio δ to see how the top wall motion controls the stability of the Poiseuille flow for different values of $\alpha \in [50,500]$ and $\delta \in [0.1,5]$. Samanta considered the linear stability of the same problem but only for $\alpha \in [50,141]$ and $\delta \in [0.1,0.6]$. A rich behavior of the system is found outside of this range of parameters. Indeed, (2) we discovered that the effect of top wall motion on the stability changes either from stabilizing to destabilizing or vice versa at certain values of wall velocity. We characterize this interesting behavior of the system by introducing a new parameter called *cutoff velocity* and studied its variation as a function of α and δ. This parameter is especially useful for industrial applications as it provides an insight on when would be economically efficient to impose a Couette component to enhance the stability, and (3) We deciphered the physics behind the stability of PCF over a permeable surface and explained the mode shift phenomenon through energy budget analysis which has never been mentioned before.

We have organized this article as follows. In Sect. 2, we define the problem mathematically and discuss the governing equations and boundary conditions. Furthermore, we derive the analytical solution for the basic (steady-state) flow. Then, in Sect. 3, we introduce planar wave perturbations to the basic state solutions to formulate a linear stability problem. The results for the linear stability analysis of plane PCF through a channel where the bottom surface is covered with porous media are presented in Sect. 4. In Sect. 5, we performed the energy budget analysis to decipher the physics behind the instabilities. Finally, we provide our conclusions in Sect. 6.

2 Problem formulation

We consider a viscous, incompressible, fully developed flow driven by a pressure gradient and a shear stress by the upper wall moving at a constant speed W. The two-dimensional fluid–porous system occupying the space $\{x \in \mathbb{R}\} \times \{y \in [-H,\ L]\}$ in which the fluid region overlies a porous medium, is shown in Fig. 1. The bottom wall is stationary. The interface between the fluid and porous layers is located at $y = 0$. We consider the porous medium to be rigid, homogenous, and isotropic with permeability κ and porosity ε.

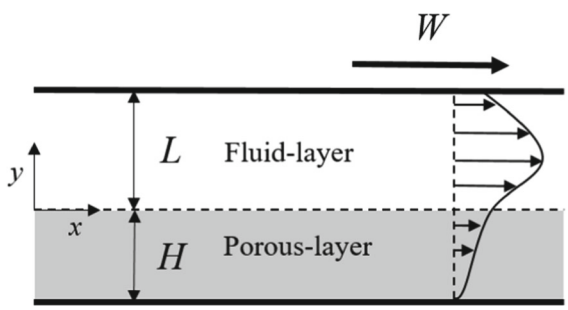

Fig. 1 Sketch of the computational domain and coordinate systems

2.1 Governing equations and boundary conditions for plane Poiseuille–Coutte flow

The flow in the fluid layer is governed by the continuity and Navier–Stokes equations:

$$\nabla \cdot \boldsymbol{u} = 0, \tag{2.1}$$

$$\frac{\partial \boldsymbol{u}}{\partial t} + \boldsymbol{u} \cdot \nabla \boldsymbol{u} = -\frac{1}{\rho}\nabla P + \frac{\mu}{\rho}\nabla^2 \boldsymbol{u}, \tag{2.2}$$

where $\boldsymbol{u} = (u, v)$, P, ρ, and μ are the fluid velocity vector, pressure, density, and dynamic viscosity, respectively.

In order to model the flow in the porous-layer, we couple the continuity and Brinkman equations stated as

$$\nabla \cdot \boldsymbol{u_m} = 0, \tag{2.3}$$

$$\frac{1}{\varepsilon}\frac{\partial \boldsymbol{u_m}}{\partial t} = -\frac{1}{\rho}\nabla P_m + \frac{\mu_e}{\rho}\nabla^2 \boldsymbol{u_m} - \frac{\mu}{\rho\kappa}\boldsymbol{u_m}. \tag{2.4}$$

The velocity and pressure have been denoted as $\boldsymbol{u_m} = (u_m, v_m)$ and P_m, respectively. The coefficient μ_e is the effective viscosity in the porous-layer which takes into the slip at the fluid–porous interface. Assuming porous media with small permeabilities, we have neglected the convection term in the Brinkman equation (2.4) similar to the previous works [9,22]. Due to lack of experimental data no exact range of permeability is known for the inertial effects to be negligible. Tilton and Cortelezzi [10] proposed a criterion. They claimed that the inertial effects can be neglected when the interface velocity is less than 5% of the mean velocity in the fluid region; however, this limit may be too generous for some porous materials. To satisfy this criterion, in current study, the minimum allowable permeability parameter is set to $\alpha_{min} = 50$.

The solution of coupled equations (2.1)–(2.4) is subject to boundary conditions at the upper and bottom walls and at the top surface of porous layer. At the upper moving wall (i.e., $y = L$) we adopt the no-slip condition given by

$$u = W, \quad v = 0. \tag{2.5}$$

At the bottom wall below the porous layer (i.e., $y_m = -H$), the velocity $\boldsymbol{u_m}$ meets the following no-slip boundary condition:

$$u_m = 0, \quad v_m = 0. \tag{2.6}$$

At the fluid–porous interface ($y = y_m = 0$), we employ the conditions proposed by Hill and Straughan [8] where the continuity of velocity, normal stress, and tangential stress is required:

$$u = u_m, \quad v = v_m, \tag{2.7}$$

$$P - 2\mu\left(\frac{\partial v}{\partial y}\right) = P_m - 2\mu_e\left(\frac{\partial v_m}{\partial y}\right), \tag{2.8}$$

$$\mu\left(\frac{\partial u}{\partial y} + \frac{\partial v}{\partial x}\right) = \mu_e\left(\frac{\partial u_m}{\partial y} + \frac{\partial v_m}{\partial x}\right). \tag{2.9}$$

Beavers and Joseph [7], Tilton and Cortelezzi [10], and Ochoa-Tapia and Whitaker [23,24] adopted different boundary conditions from ours. In their model, the continuity of pressure and the balance of tangential stresses with a jump were required in the place of Eqs. (2.8) and (2.9).

2.2 The base (steady-state) flow

The considered system is invariant to any translation along the streamwise direction. When the wall velocity and pressure gradient are small, the flow remains laminar and varies only in the transversal direction, i.e., $\boldsymbol{u} = \boldsymbol{u}(y)$, $\boldsymbol{u_m} = \boldsymbol{u_m}(y)$. By assuming a constant pressure gradient in x-direction, constant upper wall speed W and employing the boundary conditions specified above to solve Eqs. (2.1)–(2.9), one can find the velocity profile in the fluid region (i.e., $0 \le y \le 1$) as

$$u(y) = \frac{-1}{2}Cy^2 + \left(W - u_s + \frac{1}{2}C\right)y + u_s \tag{2.10}$$

and in the porous-layer ($-1 \le y_m \le 0$), the velocity profile can be stated as

$$u_m(y_m) = \frac{C}{\alpha^2\delta^2} + A_1 \mathrm{e}^{\frac{\alpha}{\sqrt{M}}y_m} + A_2 \mathrm{e}^{\frac{-\alpha}{\sqrt{M}}y_m} \tag{2.11}$$

The coefficients in Eqs. (2.10) and (2.11) are given by

$$C = \frac{-L^2}{\mu}\frac{\mathrm{d}P}{\mathrm{d}x},$$

$$u_s = u_{s_p} + u_{s_c} = \frac{\sqrt{M}C\left(\cosh\left(\frac{\alpha}{\sqrt{M}}\right) - 1\right) + \frac{1}{2}C\alpha\delta\sinh\left(\frac{\alpha}{\sqrt{M}}\right)}{\alpha^2\delta^2\sqrt{M}\cosh\left(\frac{\alpha}{\sqrt{M}}\right) + \alpha\delta\sinh\left(\frac{\alpha}{\sqrt{M}}\right)} + \frac{W\alpha\delta\sinh\left(\frac{\alpha}{\sqrt{M}}\right)}{\alpha^2\delta^2\sqrt{M}\cosh\left(\frac{\alpha}{\sqrt{M}}\right) + \alpha\delta\sinh\left(\frac{\alpha}{\sqrt{M}}\right)},$$

$$A_{1,2} = \frac{\pm\alpha\delta\,(2W + C - 2u_s)\,e^{\frac{\pm\alpha}{\sqrt{M}}} - 2\sqrt{M}C}{2\alpha^2\delta^2\sqrt{M}\left(\mathrm{e}^{\frac{\alpha}{\sqrt{M}}} + \mathrm{e}^{\frac{-\alpha}{\sqrt{M}}}\right)}. \tag{2.12}$$

Here, u_s represents the velocity at the fluid-porous interface. It should be noted that the equations in the fluid and porous layers [Eqs. (2.10)–(2.12)] have been normalized using the corresponding length scales L and H to interpret the relative magnitudes of velocity in each layer.

The base flow profile in the fluid region is the superposition of the Poiseuille flow and the Couette flow velocity profiles $u\,(y) = u_p\,(y) + u_c(y)$ where the velocity components associated with the Poiseuille and Couette flows are defined as $u_p\,(y) = \frac{-1}{2}Cy^2 - \left(u_{s_p} - \frac{1}{2}C\right)y + u_{s_p}$ and $u_c\,(y) = Wy + u_{s_c}$, respectively.

The dimensionless parameter α is the so-called permeability parameter (the reciprocal of Darcy number) $\alpha = H/\sqrt{\kappa}$ (Mirbod et al. [25]), δ is the depth ratio given by $\delta = L/H$, and the velocity ratio $U^* = W/V$ is the dimensionless wall velocity and represents the relative magnitude of the Couette component to the maximum velocity of Poiseuille flow in the fluid layer, V. The viscosity ratio is denoted by $M = \mu_e/\mu$, which is of the order of $1/\varepsilon$ (Whitaker [26]). Throughout the present investigation, we will assume $M = 1/\varepsilon$.

Before proceeding to the stability analysis, we first examine the variation of the base (steady-state) flow with the two control parameters, the depth ratio δ and the permeability parameter α. Fig. 2 shows the basic velocity profiles for different values of α, δ, and U^* with a constant porosity $\varepsilon = 0.6$. The velocity profiles in the fluid and porous layers are normalized by V. The velocity profiles are all continuous at the fluid–porous interface in contrast to the discontinuous profiles in Chang et al. [22]. The porous layer has less effects on the flow in the fluid layer (Fig. 2), as the porous layer permeability drops (i.e., for large α) and as the porous thickness reduces (i.e., for large δ) since flow is developed inside thin-porous layers. The magnitude of u_s and shear stress become even more pronounced as the Couette component U^* increases in Fig. 2a; however, for a very thin-porous medium, i.e., Fig. 2b, the slip velocity approaches zero regardless of the value of U^* since at $\alpha = 125$ and $\delta = 5$, the porous layer behaves as an impermeable wall. The same behavior can be seen in Fig. 2c–d when the permeability parameter α increases from 50 to 500. Note that in all the above cases, the maximum of velocity profile in the fluid layer shifts up towards the upper moving wall as the wall velocity increases. The instant that the maximum velocity occurs at the top wall, i.e. $u_{\max}/V = U^*$, is when the Couette flow becomes dominant.

3 Linear stability analysis

3.1 Formulation of linear stability problem

To analyze the stability, we first introduce small perturbations to the governing equations of the form

$$u = \bar{u} + \tilde{u}, \quad v = \tilde{v}, \quad P = \bar{P} + \tilde{P}, \tag{3.1}$$

$$u_m = \bar{u}_m + \tilde{u}_m, \quad v_m = \tilde{v}_m, \quad P_m = \bar{P}_m + \tilde{P}_m, \tag{3.2}$$

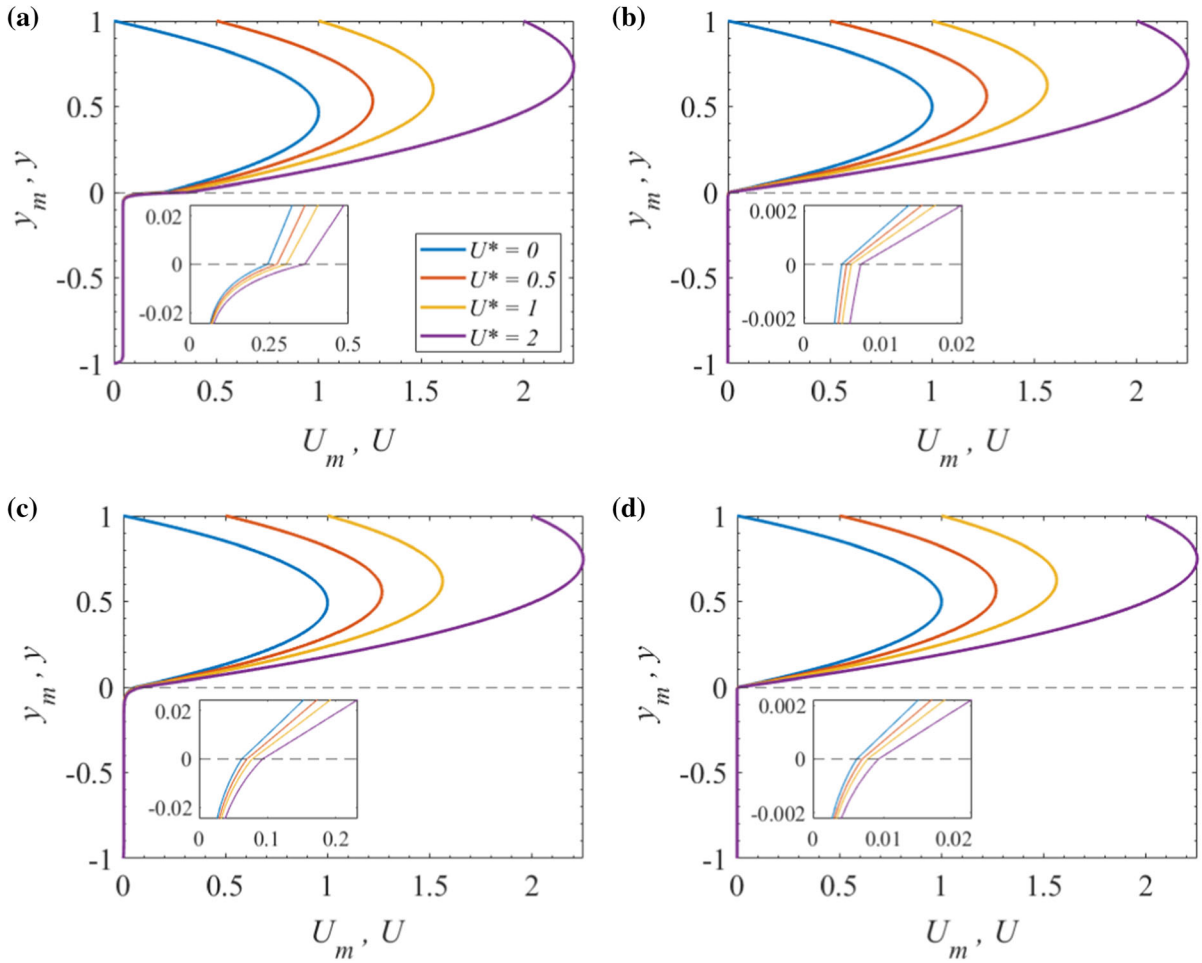

Fig. 2 The normalized base velocity profiles for different values of U^*: **a** $\alpha = 125$, $\delta = 0.1$, **b** $\alpha = 125$, $\delta = 5$, **c** $\alpha = 50$, $\delta = 1$, and **d** $\alpha = 500$, $\delta = 1$. For all cases $\varepsilon = 0.6$

Then, the equations are non-dimensionalized with length (L), velocity (V), and pressure ($\mu V/L$) scales for the fields in the fluid layer and with length (H), velocity (V_m), and pressure ($\mu V_m/H$) for the fields in the porous layer. The time is scaled with L/V for both layers. Here, V and V_m are the maximum velocities in the fluid and porous layers.

Finally, we linearize Eqs. (2.1)–(2.10) to obtain the equations governing the linear dynamics of perturbations as

$$\frac{\partial \tilde{u}}{\partial x} + \frac{\partial \tilde{v}}{\partial y} = 0, \tag{3.3}$$

$$\mathrm{Re}\left(\frac{\partial \tilde{u}}{\partial t} + U\frac{\partial \tilde{u}}{\partial x} + \tilde{v}\frac{\partial U}{\partial x}\right) = -\frac{\partial \tilde{P}}{\partial x} + \nabla^2 \tilde{u}, \tag{3.4}$$

$$\mathrm{Re}\left(\frac{\partial \tilde{v}}{\partial t} + U\frac{\partial \tilde{v}}{\partial x}\right) = -\frac{\partial \tilde{P}}{\partial y} + \nabla^2 \tilde{v}, \tag{3.5}$$

$$\frac{\partial \tilde{u}_m}{\partial x_m} = 0, \tag{3.6}$$

$$\mathrm{Re}_m\left(\frac{\partial \tilde{u}_m}{\partial t_m}\right) = -\frac{\partial \tilde{P}_m}{\partial x_m} + M\nabla^2 \tilde{u}_m - \alpha^2 \tilde{u}_m, \tag{3.7}$$

$$\mathrm{Re}_m\left(\frac{\partial \tilde{v}_m}{\partial t_m}\right) = -\frac{\partial \tilde{P}_m}{\partial y_m} + M\nabla^2\tilde{v}_m - \alpha^2\tilde{v}_m, \tag{3.8}$$

where U is the velocity field of the basic flow. The Reynolds number in the fluid and porous regions are defined as $\mathrm{Re} = \rho V L/\mu$ and $\mathrm{Re}_m = \rho V_m H/\mu$, respectivley. We then assume the disturbances have wave-like forms as follows:

$$(\tilde{u},\ \tilde{v},\ \tilde{P}) = \left(\hat{u}\,(y)\,,\ \hat{v}\,(y)\,,\ \hat{P}\,(y)\right)\exp\left[\mathrm{i}k\,(x - st)\right], \tag{3.9}$$

$$(\tilde{u}_m,\ \tilde{v}_m,\ \tilde{P}_m) = \left(\hat{u}_m\,(y)\,,\ \hat{v}_m\,(y)\,,\ \hat{P}_m\,(y)\right)\exp\left[\mathrm{i}k_m\,(x_m - s_m t)\right]. \tag{3.10}$$

The perturbations travel in x-direction with streamwise wavenumber k in the fluid region and k_m in the porous region. In this study, we use temporal linear stability analysis where wavenumbers are real whereas phase velocities $s = s_r + \mathrm{i}s_\mathrm{i}$ and $s_m = s_{m_r} + \mathrm{i}s_{m_\mathrm{i}}$ are complex whose real parts represent the phase speeds and imaginary parts determine the growth/decay rate depending on the sign. The system is unstable when $s_\mathrm{i} > 0$. The wavenumbers, Reynolds numbers, and temporal growth rates in the two layers are related by

$$k = k_m\delta, \quad \mathrm{Re}_m = \zeta\delta\mathrm{Re}, \quad s\mathrm{Re} = \delta s_m\,\mathrm{Re}_m \tag{3.11}$$

Here, ζ is the ratio V_m/V. By substituting Eqs. (3.9) into (3.3)–(3.5), we can then obtain the normal modes equations for the fluid region ($0 \le y \le 1$) as

$$\mathrm{i}k\hat{u} + D\hat{v} = 0, \tag{3.12}$$

$$\mathrm{Re}(-\mathrm{i}ks\hat{u} + U\mathrm{i}k\hat{u} + \hat{v}U') = -\mathrm{i}k\hat{P} + (D^2 - k^2)\hat{u}, \tag{3.13}$$

$$\mathrm{Re}(-\mathrm{i}ks\hat{v} + U\mathrm{i}k\hat{v}) = -D\hat{P} + (D^2 - k^2)\hat{v}. \tag{3.14}$$

Similarly, for the porous region ($-1 \le y_m \le 0$) we have

$$ik_m\hat{u}_m + D_m\hat{v}_m = 0, \tag{3.15}$$

$$\mathrm{Re}_m\left(-\frac{\mathrm{i}k_m}{\varepsilon}s_m\hat{u}_m\right) = -\mathrm{i}k_m\hat{P}_m + M\left(D_m^2 - k_m^2\right)\hat{u}_m - \alpha^2\hat{u}_m, \tag{3.16}$$

$$\mathrm{Re}_m\left(-\frac{\mathrm{i}k_m}{\varepsilon}s_m\hat{v}_m\right) = -D_m\hat{P}_m + M\left(D_m^2 - k_m^2\right)\hat{v}_m - \alpha^2\hat{v}_m, \tag{3.17}$$

where $D = \mathrm{d}/\mathrm{d}y$, $D^2 = \mathrm{d}^2/\mathrm{d}y^2$, $D_m^2 = \mathrm{d}^2/\mathrm{d}y_m^2$ and $U' = \mathrm{d}U/\mathrm{d}y$. The boundary conditions will be also stated as

$$\text{at } y = 1 \quad \hat{u} = 0, \quad \hat{v} = 0, \tag{3.18}$$

$$\text{at } y_m = -1 \quad \hat{u}_m = 0, \quad \hat{v}_m = 0, \tag{3.19}$$

$$\begin{aligned} &\text{at } y = y_m = 0 \hat{u} = \zeta\hat{u}_m,\ \hat{v} = \zeta\hat{v}_m,\\ &D\hat{u} + \mathrm{i}k\hat{v} = \delta M\zeta(D_m\hat{u}_m + \mathrm{i}k\hat{v}_m),\\ &\hat{P} - 2D\hat{v} = \delta\zeta\hat{P}_m - 2\delta M\zeta D_m\hat{v}_m. \end{aligned} \tag{3.20}$$

Equations (3.12)–(3.17) with the boundary condition (3.18)–(3.20) form an eigenvalue problem which can be solved by transforming the equations to the Chebyshev domain (cf. Dolapci [27] and Makinde [28]). To do so, we approximate the perturbation amplitude function using Chebyshev expansion.

$$\hat{X}\,(\xi) = \sum_{n=0}^{N}\hat{X}_n T_n\,(\xi)\,, \tag{3.21}$$

where T_n is the Chebyshev polynomial of degree n. The variable ξ ($\in [-1,\ 1]$) is related to y by $\xi = 2y - 1$ for velocity and pressure fields in the fluid layer and to y_m by $\xi = 2y_m + 1$ for the fields in the porous layer. By applying Eq. (3.21) for $\hat{u}$, $\hat{v}$, $\hat{P}$, $\hat{u}_m$, $\hat{v}_m$, and $\hat{P}_m$ in Eqs. (3.12)–(3.20) and implementing QZ algorithm, one can calculate the related eigenvalues. The highest degree of considered Chebyshev polynomials are set to $N = 75$ for convergence. (See Appendix A for the details on the N determination.)

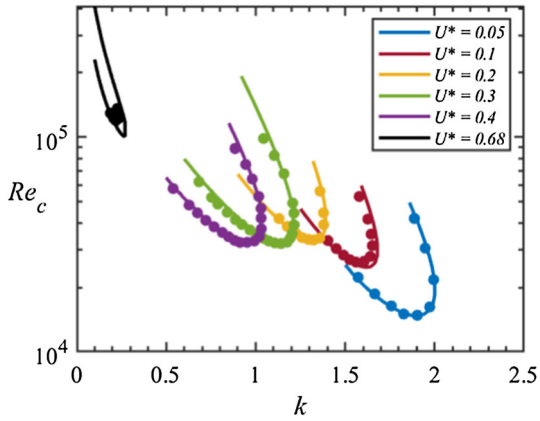

Fig. 3 Neutral curves for the plane PCF with impermeable walls for different wall velocity U^*. The solid lines represent the present results and the solid circles represent the results by Potter [16]

3.2 Validation of the numerical method

To validate our numerical method, we consider plane PCF with an impermeable porous layer, by setting $\varepsilon \to 0$, and determine neutral stability curves for different upper wall velocities. We compare the results with the work by Potter [16]. We found that there is a close agreement between our results (solid lines in Fig. 3) and Potter's results (dots in Fig. 3). The flow becomes more stable as the upper wall velocity increases except for $0.2 < U^* < 0.4$. According to Potter [16], this effect is produced because U^* is approximately equal to the streamwise phase speed s_r and the point where $U^* = s_r$ seems to be the inflexion point. Figure 3 also shows that as the U^* approaches to 0.7, the critical Reynolds number approaches infinity and the critical wavenumber becomes zero. It can be concluded that the Couette flow becomes dominant when $U^* > 0.7$, hence, the flow is unconditionally stable to infinitesimal perturbations for all Reynolds numbers [29].

4 Linear stability analysis results and discussion

4.1 Eigenvalues spectra

We solved the eigenvalue problem and plotted the eigenvalue spectra for flows over porous media. Figure 4 illustrates the behavior of eigenvalues when the wall velocity U^* is increased from 0 to 2, for different values of α, and δ. The porosity is fixed at $\varepsilon = 0.6$. The circled eigenvalues in Fig. 4 correspond to $U^* = 0$ (i.e., plane PF). It can be seen that the circled eigenvalues consist of two main branches; the right branch have a Y-shaped arrangement and the left branch is a near-vertical line with phase speed s_r around zero. The eigenvalues in the left branch are the so-called *porous modes* since the associated eigenfunctions vary only in the porous region [10].

In Fig. 4a, for $\alpha = 50$, only two modes can become unstable depending on U^*. As the wall velocity U^* gradually increases from 0, initially unstable mode 1 becomes stable and initially stable mode 2 becomes unstable. The base of the right branch eigenvalues (the near-vertical line in the Y-shaped spectrum) shifts to the right as U^* approaches to 2. For small permeability or large velocity ratio, e.g., the case of $\alpha = 500$, shown in Fig. 4b, the modes 1 and 2 do not cross the real axis, shown by a red dashed-line; meaning that the disturbances are dampened regardless of the magnitude of the Couette component. The trajectory of mode 2 suggests that the Couette component first destabilizes the flow and when $U^* > 1.1$, it starts stabilizing the flow. It can also be seen in Fig. 4b that the *porous mode* disappears since the porous layer behaves almost as an impermeable solid wall.

The eigenvalues trajectories in Fig. 4c show that for $\alpha = 125$ and $\delta = 0.1$, the Poiseuille flow with $\mathrm{Re} = 3000$ and $k = 1$ is unstable since there is an eigenvalue with a positive imaginary part. Further increasing U^*, makes mode 1 to move further away from the real axis; hence, causing fast growth of flow disturbances. Many eigenvalues in the porous branch have damping rates close to 0 and the decaying disturbances survive for a long time due to the porous layer.

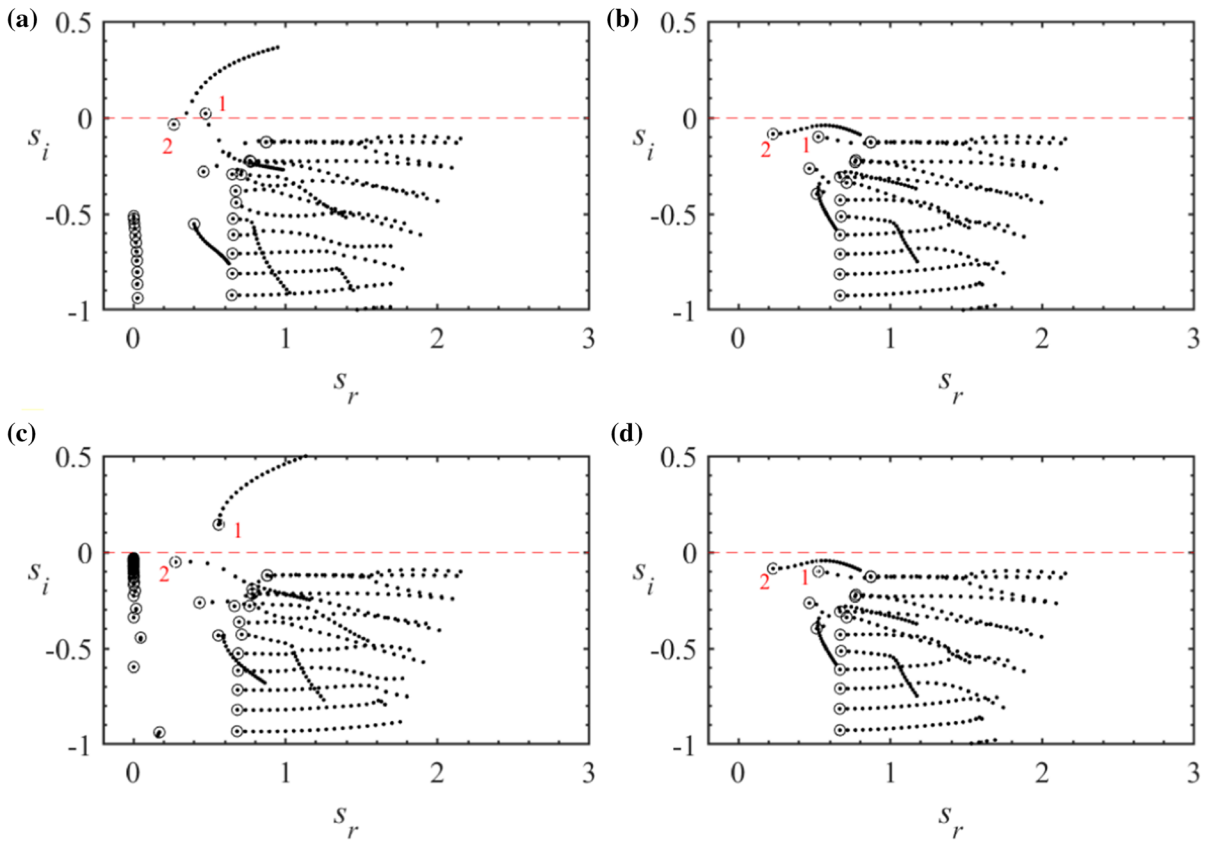

Fig. 4 Variation of eigenvalue spectrum for Re $= 3000$, $k = 1$, and $\varepsilon = 0.6$ with velocity ratio increasing from $U^* = 0$ (indicated by open circles) to $U^* = 2$: **a** $\alpha = 50$, $\delta = 1$, **b** $\alpha = 500$, $\delta = 1$, **c** $\alpha = 125$, $\delta = 0.1$, and **d** $\alpha = 125$, $\delta = 5$

The spectrum plotted in Fig. 4d is similar to Fig. 4b. This suggests that for relatively large values of thickness ratio (i.e., $\delta = 5$) and permeability parameter, as the velocity ratio increases, the disturbances are dampened regardless of the magnitude of the Couette component. In addition, the disappearance of *porous mode* in these two figures suggests the little importance of porous layer effects in stability of the flow when α and δ have moderate values.

4.2 The effect of permeability parameter α on linear stability

To analyze the effect of permeability parameter α on the stability of plane PCF for different velocity ratio U^*, we varied α where other porous parameters kept constant at $\delta = 1$ and $\varepsilon = 0.6$. Figure 5 illustrates the variation of neutral stability curves with different U^* and various permeability parameters of $\alpha = 50$, 75, 100, and 500. When the Couette flow is absent, neutral curves display a bi-modal behavior with a global minimum in the short-wave branch (right branch) and a local minimum in the long-wave branch (left branch) (Worster [30]; Liu et al. [9]; Chang et al. [6]). The short-wave branch is referred to as the fluid mode and the long-wave branch is the porous mode. Figure 5a–b shows that the increase of Couette flow component is accompanied by the disappearance of the porous mode and destabilization of the fluid mode. Similar behavior can be seen in Fig. 5c; however, at $U^* \approx 1.1$ the Couette flow starts exerting the stabilizing effect. Figure 5d shows that for large permeability parameter $\alpha = 500$, the Couette flow, even for small values of U^*, stabilizes the flow. Also, a mode-shift from the short-wave branch to the long-wave branch, i.e. the porous branch, occurs at larger values of α when the velocity ratio varies from $U^* = 0.5$ to $U^* = 1$ where the porous branch controls the onset of instability. At $U^* = 2$ two mode shifts happen;

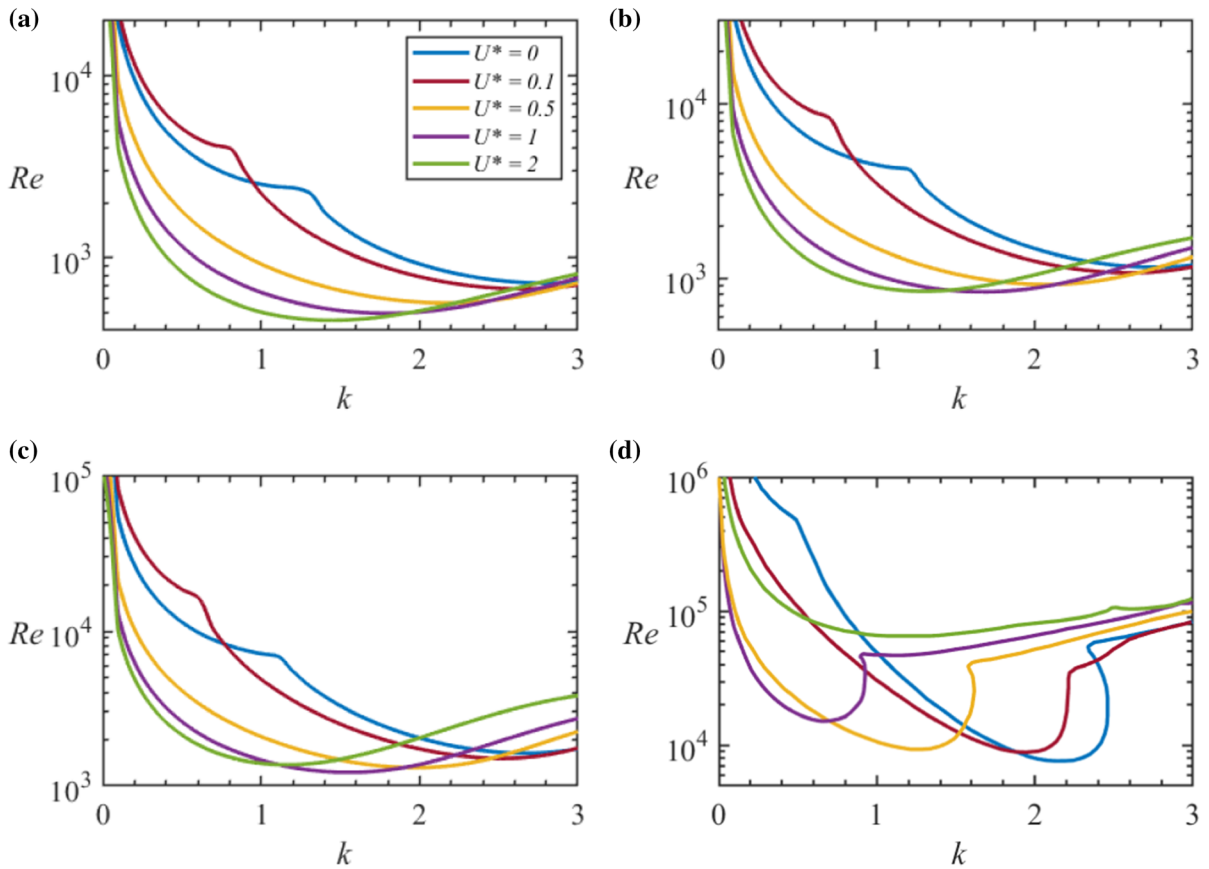

Fig. 5 The variation of neutral curves with velocity ratio U^* at different values of permeability: **a** $\alpha = 50$, **b** $\alpha = 75$, **c** $\alpha = 100$, and **d** $\alpha = 500$. For all cases $\delta = 1$ and $\varepsilon = 0.6$

(1) the mode shifts from the fluid branch to the porous branch and, (2) once α is increased passed 200 the second mode shift from porous branch to fluid branch occurs.

4.3 The effect of depth ratio parameter δ on linear stability

To investigate the effect of depth ratio δ on the stability of plane PCF, we repeated the analysis of Sect. 4.2. for $\delta = 0.1, 0.5, 1$ and 5, maintaining constant $\alpha = 125$ and $\varepsilon = 0.6$. In general, a bi-modal structure can be found in the neutral curves corresponding to a PF ($U^* = 0$). However, as U^* increases the shape of neutral curve becomes monomodal. Figure 6a–b shows that the critical Reynolds number reduces as the upper wall velocity increases. In Fig. 6c, for $\delta = 1$, similar to Fig. 5c, as the velocity ratio increases the flow first destabilized and then stabilized. Finally, the neutral curves in Fig. 6d show that imposing Couette component on the PF over a thin-porous medium would considerably stabilize the flow. In all four cases considered herein, the instability shifts from a short-wave mode to a long-wave mode with increasing U^*. However, for the case $\delta = 5$, the instability shifts back toward short-wave mode at high upper wall velocities.

To further characterize the impact of Couette component in the flow, in Fig. 7a–b the variation of the critical Reynolds number Re_c with permeability parameter α and depth ratio δ have been illustrated at different values of the velocity ratio U^*. Figure 7 shows that increasing α or δ enhances the stability of the system regardless of the value of U^*. Imposing a Couette flow to a plane Poiseuille flow over a porous surface produces destabilizing effects at small α and δ and significant stabilizing effects at large α and δ. For example, if the permeability parameter of

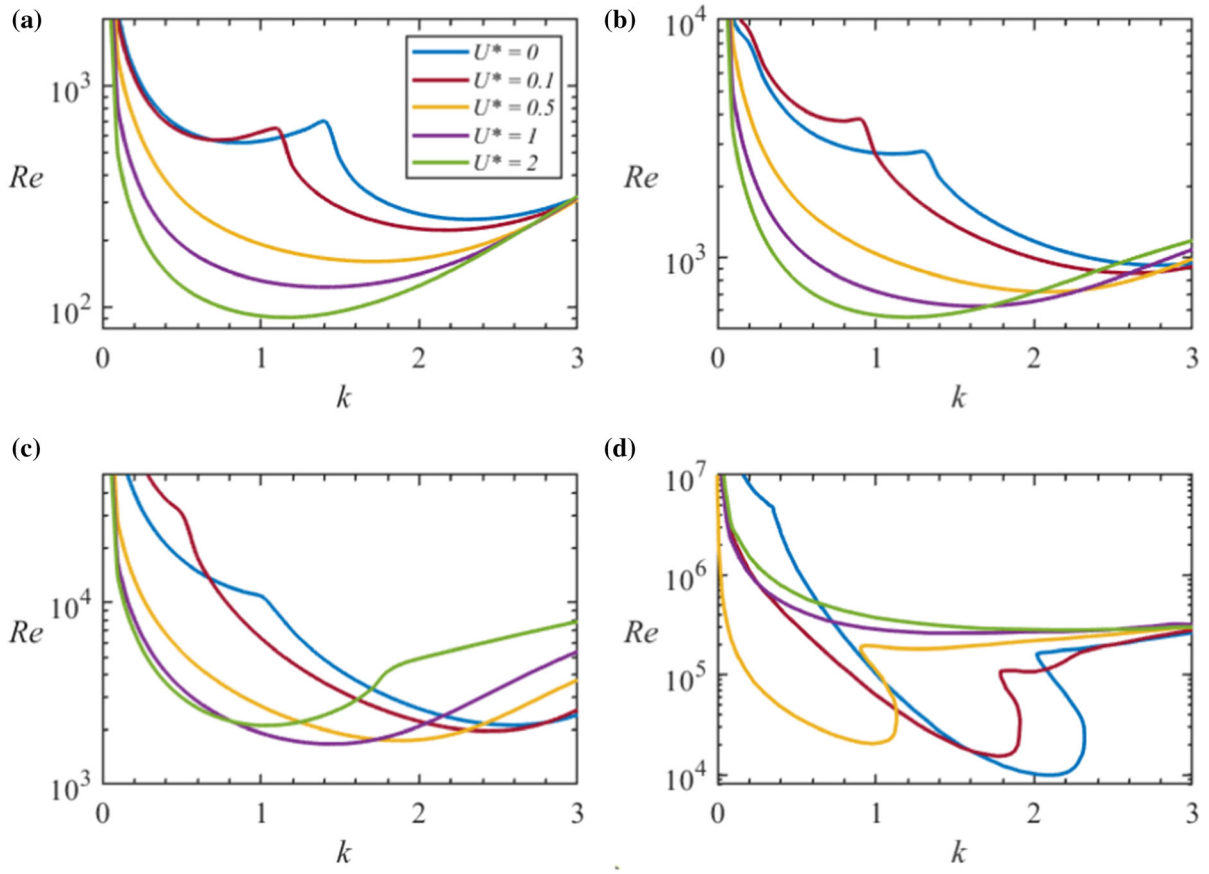

Fig. 6 The variation of neutral curves with velocity ratio U^* at different values of depth ratio: **a** $\delta = 0.1$, **b** $\delta = 0.5$, **c** $\delta = 1$, and **d** $\delta = 5$. For all cases $\alpha = 125$ and $\varepsilon = 0.6$

a porous surface is $\alpha = 100$ and $\delta = 1$, it is recommended to not incorporate a Couette flow in the system for the stability of laminar flow; however, for a different porous surface with $\alpha = 400$, adding a Couette component would help achieving a more stable flow.

4.4 Eigenfunctions and streamlines

To further explore the characteristic of the instability, we analyze the eigenfunctions by visualizing streamfunctions ϕ and ϕ_m and streamlines of critical modes, as displayed in Figs. 8 and 9. The streamfunctions have been normalized by the maximum of their magnitude. In Fig. 8a for $\alpha = 50$, $U^* = 0$ (i.e., PF), the magnitude of the streamfunction peaks near the center of the fluid layer and it gradually decreases as it approaches the interface and the bottom stationary wall. This results in the generation of vortices that mostly occupy the fluid layer and slightly penetrate into the porous layer; therefore, we can conclude that the disturbances in the fluid layer trigger the instability. Once the Couette flow is imposed to the system, as shown in Fig. 8b for $\alpha = 50$, $U^* = 2$, the magnitude of the streamfunction in the porous layer φm increases due to an increase in the basic state interface velocity. Hence, the perturbation flows penetrate more into the porous layer as the wavelength increases simultaneously. Figure 8c for $\alpha = 500$, $U^* = 0$ shows perturbation flow is compacted inside the fluid layer when the permeability is very small, and the porous layer behaves like an impermeable wall.

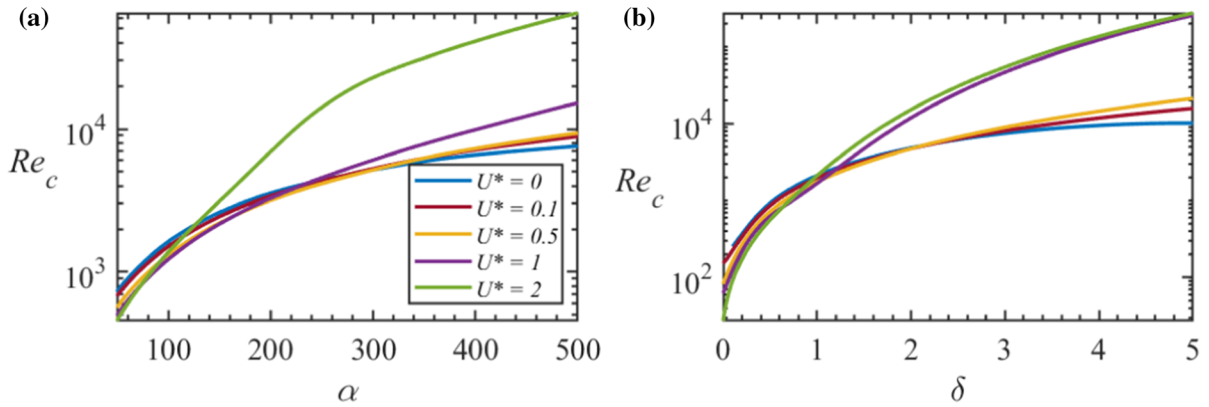

Fig. 7 The variation of critical Reynolds number Re_c with **a** permeability parameter α and **b** depth ratio δ at different values of velocity ratio U^*. For all cases $\varepsilon = 0.6$

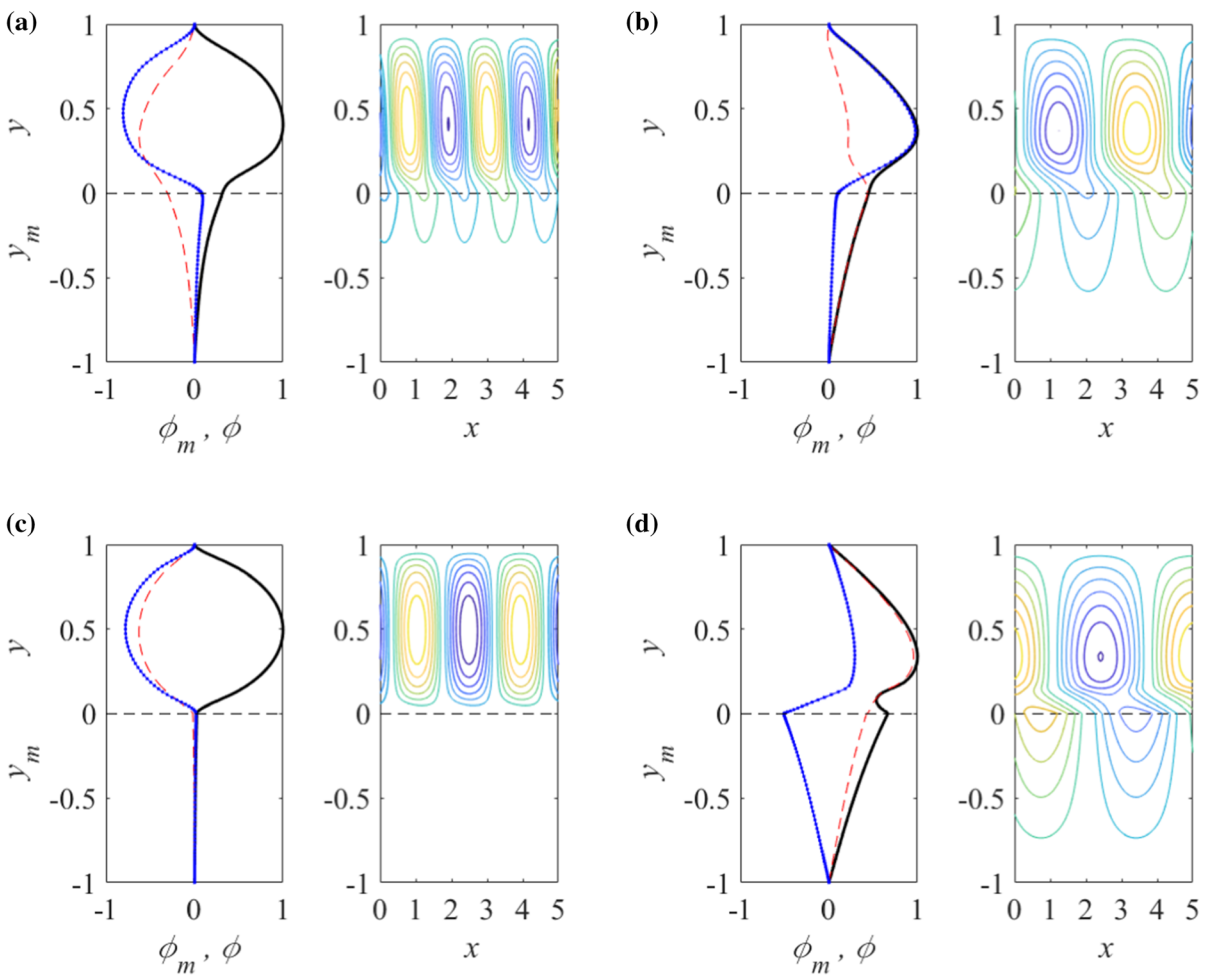

Fig. 8 Perturbation flow fields of critical modes. Profiles of streamfunctions (left panel) and streamlines (right panel) for different parameter values: **a** $\alpha = 50$, $U^* = 0$, **b** $\alpha = 50$, $U^* = 2$, **c** $\alpha = 500$, $U^* = 0$, **d** $\alpha = 500$, $U^* = 2$. The other parameters are $\delta = 1$ and $\varepsilon = 0.6$. Solid, dashed, and dash-dotted lines represent the magnitude, real, and imaginary parts of the streamfunctions, respectively

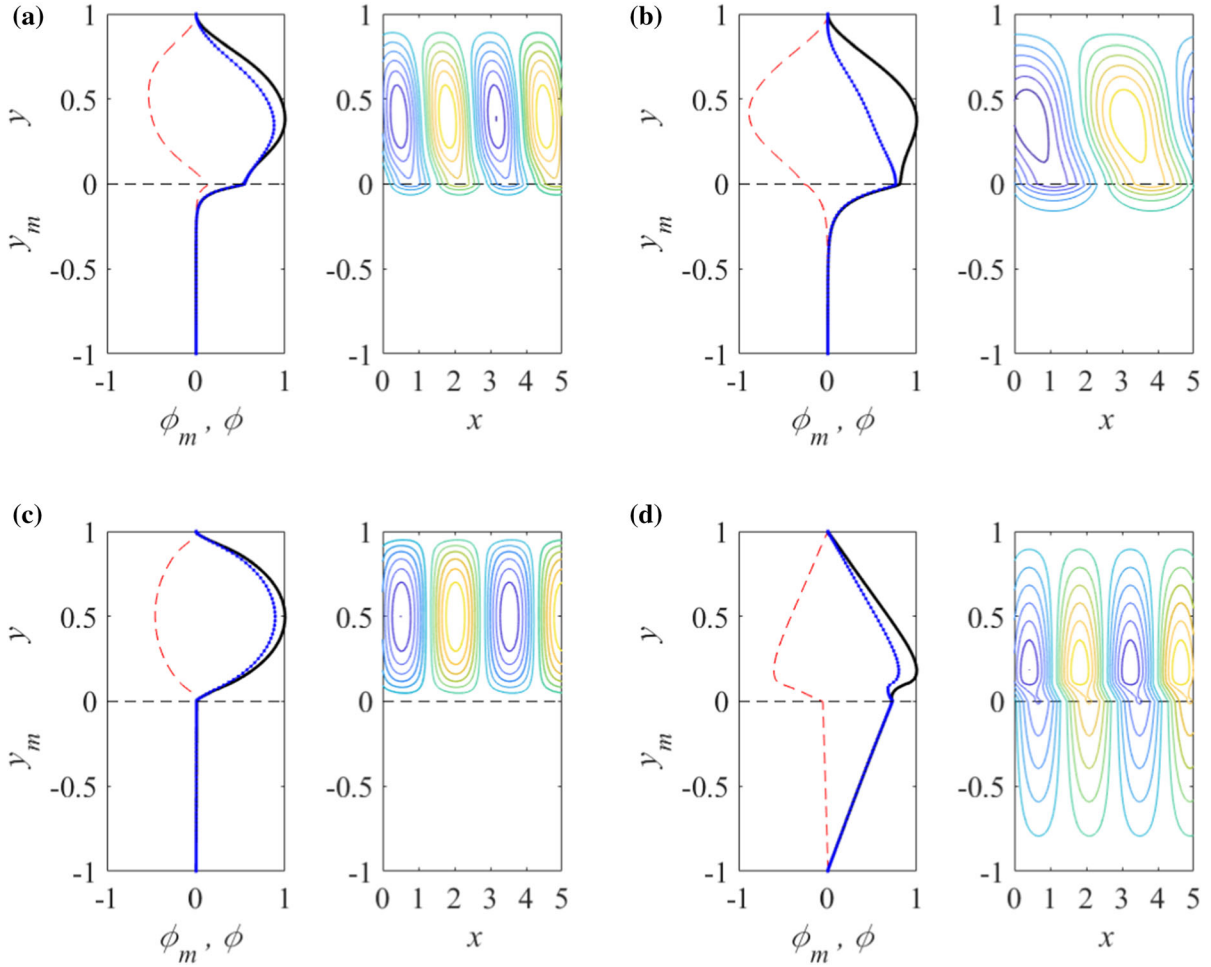

Fig. 9 Perturbation flow fields of critical modes. Profiles of streamfunctions (left panel) and streamlines (right panel) for different parameter values: **a** $\delta = 0.1$, $U^* = 0$, **b** $\delta = 0.1$, $U^* = 2$, **c** $\delta = 5$, $U^* = 0$, **d** $\delta = 5$, $U^* = 2$. The other parameters are $\alpha = 125$ and $\varepsilon = 0.6$. Solid, dashed, and dash-dotted lines represent the magnitude, real, and imaginary parts of the eigenfunctions, respectively

The profile of magnitude of ϕ is even-symmetric with respect to the center line of the fluid layer that corresponds to the so-called even-fluid-layer by Chang et al. [6]. It can be observed in Fig. 8d for $\alpha = 50$, $U^* = 2$ that when $U^* = 2$, a rapid change in the magnitude of ϕ occurs near the interface which leads to occurrence of small vortices there. This is the case where the porous layer controls the onset of stability as was discussed in Sect. 4.2.

Furthermore, we analyzed the eigenfunction profiles and streamlines in Fig. 9 to provide insight on what mode controls the stability by varying the depth ratio with the existence of a Couette component in the system. For the cases shown in Fig. 9a, b, the instability is triggered by the disturbances in the fluid layer since perturbation flow is concentrated within the fluid layer. Increasing the upper wall velocity causes the interface velocity of the basic state increases, as shown in Fig. 2; consequently, results in more penetration of streamlines into the porous layer. However, once the depth ratio increases to $\delta = 5$, see Fig. 9c, the disturbances are contained within the fluid layer and are vanished inside the porous layer. The eigenfunction in Fig. 9c is symmetric with respect to the fluid layer center line and for that reason it is called even-fluid-layer by Chang et al. [6]. The small fluctuation near the interface in the profile of ϕ in Fig. 9d, $\delta = 5$ and $U^* = 2$, implies the formation of vortices at the fluid–porous interface. The secondary vortex motion on the streamline patterns intensifies by a rapid fluctuation near the interface. It should be noted that

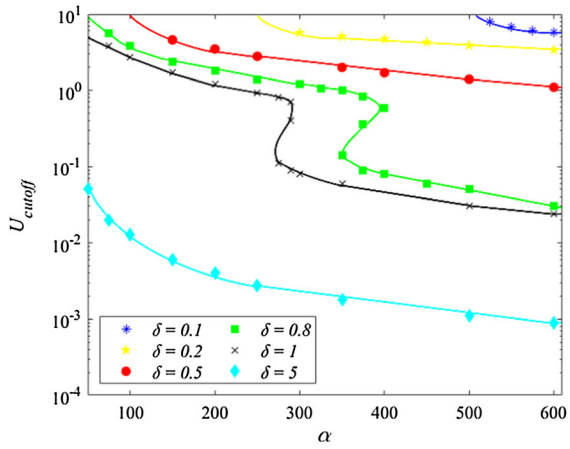

Fig. 10 The variation of wall cutoff velocity U_{cutoff}, vs. permeability α for different depth ratio δ

although the existence of a porous surface generates vortices near and inside the porous layer, the flow stability is still dominated by the fluid layer because the intensity of flow patterns is still higher in the fluid layer than the porous layer.

4.5 Variation of cutoff velocity U_{cutoff}, with α and δ

We have seen in Figs. 5, 6, and 7 that imposing a Couette flow to the system exerts destabilizing effects initially, but as the Couette component increases the flow eventually starts stabilizing. U_{cutoff} is defined as the wall velocity at which the imposed Couette flow does not affect the stability of PF over a permeable surface. In other words, the critical Reynolds number is the same for both PCF and PF when the wall velocity is equal to U_{cutoff}. In order to enhance the stability of a Poiseuille flow over a permeable surface by imposing a Couette component U^*, the magnitude of U^* must be greater than U_{cutoff}. Figure 10 illustrates the variation of U_{cutoff} with α for different depth ratios ranging from $\delta = 0.1$ to $\delta = 5$. It can be seen that U_{cutoff} decreases significantly as the depth ratio increases. For instance, in order to improve the stability of the Poiseuille flow over a porous surface with permeability parameter $\alpha = 500$ (i.e., low porous permeability), the value of U_{cutoff} is 5.8 for $\delta = 0.2$ while its value drops to 0.0011 when $\delta = 5$. Figure 10 reveals that U_{cutoff} also reduces as the porous-layer approaches to an impermeable wall. Note that for small depth ratios and very low permeabilities, adding a Couette flow has stabilizing effect. In general, these results show that the choice of coupling Couette and Poiseuille flows to improve stability of the two-layer system significantly depends on the properties (i.e., permeability and porosity) and the thickness of the porous-layer.

As shown in Fig. 10, the cutoff velocity is multivalued for some combinations of permeabilities and depth ratios, e.g., at $\alpha = 275$ and $\delta = 1$, the cutoff velocity takes two values $U_{cutoff} = 0.11$ and 0.8. This strange behavior of U_{cutoff} in these cases suggests that as the imposed Couette flow increases, the stability enhances temporarily for a range of small Couette components and then indefinitely when the Couette component exceeds the upper value of U_{cutoff}.

The significance of cutoff velocity can be exploited in accordance with the relevant applications involving flows over porous materials such as Foametal B and Aloxite. Ochoa-Tapia and Whitaker [23] indicated the permeability of above materials as $\kappa_F = 3.93 \times 10^{-8}$ m^2 and $\kappa_A = 1.6 \times 10^{-9}$m^2, respectively. Assuming the depth ratio $\delta = 1$ with the porous layer thickness $H = 2 \times 10^{-2}$ m^2, the corresponding permeability parameters read $\alpha_F = 101$ and $\alpha_A = 500$. In order to enhance the stability of a Poiseuille flow over and through a Foametal B substrate by imposing a Couette flow, U_{cutoff} should be set greater than about 2.7; whereas, for an Aloxite substrate the U_{cutoff} is required to be around 0.03. This analysis reveals that coupling a Couette component with a Poiseuille flow is economically justified in certain applications. It should be noted that due to consideration of continuity of tangential stress at the fluid–porous interface, the momentum coefficient τ proposed by Beavers and Joseph [7] and Ochoa-Tapia and Whitaker [23,24] is assumed to be zero for Aloxite.

5 Energy budget analysis

To get a better understanding of the physics behind the flow instabilities observed in the previous section, we performed energy budget analysis following Lin [31], Kelly et al. [32], and Ghosh et al. [33]. The energy budget terms for small disturbances induced in the system is obtained as follows. We first multiplied the linearized perturbed momentum equation by its respective streamwise and normal velocity components and averaged over wavelength $\lambda = 2\pi/k$. We integrated them over fluid layer depth; then, substituted the continuity equation and boundary conditions to obtain the rate of change of the kinetic energy in the fluid layer

$$\frac{\mathrm{d}K}{\mathrm{d}t} = W_p + W_v + W_{\mathrm{Re}} - D, \tag{5.1}$$

where,

$$K = \int_0^1 \left\langle \frac{\rho}{2}\left(\tilde{u}^2 + \tilde{v}^2\right)\right\rangle \, \mathrm{d}y, \tag{5.2}$$

$$W_p = \frac{1}{\mathrm{Re}} \langle \tilde{p}\tilde{v}\rangle_{y=0}, \tag{5.3}$$

$$W_v = -\frac{1}{\mathrm{Re}} \left\langle \mu\left(\frac{\partial \tilde{v}}{\partial x} + \frac{\partial \tilde{u}}{\partial y}\right)\tilde{u} + 2\mu\frac{\partial \tilde{v}}{\partial y}\tilde{v}\right\rangle_{y=0}, \tag{5.4}$$

$$W_{\mathrm{Re}} = -\int_0^1 \left\langle \rho\tilde{u}\tilde{v}\frac{\mathrm{d}U}{\mathrm{d}y}\right\rangle \, \mathrm{d}y, \tag{5.5}$$

$$D = \frac{1}{\mathrm{Re}}\int_0^1 \left\langle 2\mu\left(\frac{\partial \tilde{u}}{\partial x}\right)^2 + \mu\left(\frac{\partial \tilde{u}}{\partial y} + \frac{\partial \tilde{v}}{\partial x}\right)^2 + 2\mu\left(\frac{\partial \tilde{v}}{\partial y}\right)^2\right\rangle \mathrm{d}y. \tag{5.6}$$

Here, the operator $\langle \bullet \rangle = \frac{1}{\lambda}\int_0^\lambda \bullet \, \mathrm{d}x$ denotes the averaging operation over the wavelength in the fluid layer. The term $\mathrm{d}K/\mathrm{d}t$ on the left-hand-side (LHS) of Eq. (5.1) represents the rate of increase of the spatially averaged kinetic energy of perturbation flow in the fluid layer, K. The terms W_p and W_v represent the powers of pressure force and shear stress exerted by the flow in the porous layer, respectively. W_{Re} is the power of Reynolds stress and D represents the rate of viscous energy dissipation in the fluid layer.

Similarly, the rate of change of kinetic energy in the porous layer can be obtained as

$$\frac{\mathrm{d}K_m}{\mathrm{d}t_m} = W_{p_m} + W_{v_m} - G_m - D_m, \tag{5.7}$$

where

$$K_m = \zeta^3 \int_{-1}^0 \left\langle \frac{\rho}{2\varepsilon}\left(\tilde{u}_m^2 + \tilde{v}_m^2\right)\right\rangle_m \, \mathrm{d}y_m, \tag{5.8}$$

$$W_{p_m} = \frac{\zeta^2\delta}{\mathrm{Re}} \langle \tilde{p}_m\tilde{v}_m\rangle_{m_{y_m=0}}, \tag{5.9}$$

$$W_{v_m} = -\frac{\varepsilon\zeta^2\delta}{\mathrm{Re}} \left\langle \left(\frac{\partial \tilde{v}_m}{\partial x_m} + \frac{\partial \tilde{u}_m}{\partial y_m}\right)\tilde{u}_m + 2\frac{\partial \tilde{v}_m}{\partial y_m}\tilde{v}_m\right\rangle_{m_{y_m=0}}, \tag{5.10}$$

$$G_m = \frac{\varepsilon\alpha^2\delta^2\zeta^3}{\mathrm{Re}} \int_{-1}^0 \left\langle \tilde{u}_m^2 + \tilde{v}_m^2\right\rangle_m \, \mathrm{d}y_m, \tag{5.11}$$

$$D_m = \frac{\varepsilon\zeta^2\delta^2}{\mathrm{Re}} \int_{-1}^0 \left\langle 2\left(\frac{\partial \tilde{u}_m}{\partial x_m}\right)^2 + \left(\frac{\partial \tilde{u}_m}{\partial y_m} + \frac{\partial \tilde{v}_m}{\partial x_m}\right)^2 + 2\left(\frac{\partial \tilde{v}_m}{\partial y_m}\right)^2\right\rangle_m \mathrm{d}y_m, \tag{5.12}$$

Here, the term $\mathrm{d}K_m/\mathrm{d}t_m$ on the left-hand-side (LHS) of Eq. (5.8) represents the rate of increase of the spatially averaged kinetic energy of perturbation flow in the porous layer, K_m. The terms W_{p_m} and W_{v_m} represent the powers of pressure force and shear stress exerted by the flow in the fluid layer. G_m is the rate of viscous energy dissipation due to pores, and D_m represents the rate of viscous energy dissipation in the porous layer.

Combining Eqs. (5.1) and (5.7), the total rate of change of kinetic energy of the whole system is given as

$$\frac{\mathrm{d}K}{\mathrm{d}t} + \frac{\mathrm{d}K_m}{\mathrm{d}t_m} = W_p + W_v + W_{\mathrm{Re}} - D + W_{p_m} + W_{v_m} - G_m - D_m. \tag{5.13}$$

It should be emphasized that since K and K_m are both proportional to $\mathrm{e}^{2s_i t}$, the left-hand side of Eq. (5.13) can be calculated as

$$\frac{\mathrm{d}K}{\mathrm{d}t} + \frac{\mathrm{d}K_m}{\mathrm{d}t_m} = 2s_i(K + K_m). \tag{5.14}$$

Hence, the system can be unstable (LHS $>$ 0), neutrally stable (LHS $=$ 0), or stable (LHS $<$ 0) depending on the evolution of kinetic energy with time. By substituting Eq. (5.14) into Eq. (5.13) and normalizing both sides by $2(K + K_m)$, we obtain

$$s_i = W_p' + W_v' + W_{\mathrm{Re}}' - D' + W_{p_m}' + W_{v_m}' - G_m' - D_m'. \tag{5.15}$$

For simplicity, we drop the ($'$) from now on. Also, from continuity of normal and tangential stresses at the interface, we have $W_p + W_v + W_{\mathrm{Re}} + W_{p_m} + W_{v_m} = 0$; therefore, Eq. (5.15) is simplified to

$$s_i = W_{\mathrm{Re}} - D - G_m - D_m. \tag{5.16}$$

To study the effect of varying permeability parameter α, depth ratio δ, and Couette component U^* on the stability, we compute the energy budget terms in Eq. (5.16). Figure 11 shows numerical values of budget terms with wavenumber at Re $=$ 1000 for three different cases, Case 1: $\alpha = 125, \delta = 1$, Case 2: $\alpha = 50, \delta = 1$, and Case 3: $\alpha = 125, \delta = 0.1$. The Couette flow is absent in all three cases (i.e., $U^* = 0$). Neutral stability curves for these cases and the growth rates computed at Re $=$ 1000 are also shown as a reference. The Reynolds stress against the base flow shear produces the required energy for the disturbances to grow, meaning, W_{Re} is the only production term. The rate of viscous energy dissipation due to the pores of the porous layer (G_m) and the rate of viscous energy dissipation in the fluid and porous layers (D and D_m) are considered to be negative. One key point that can be seen in Fig. 11a–b is that the trends of variation of s_i and W_{Re} are very similar except that the growth rates are shifted down due to viscous energy dissipation. Therefore, it is safe to say that Reynolds stress plays an important role in controlling the stability which subsequently makes the fluid layer to dominate the stability of the system. In order to investigate the effect of permeability parameter on the stability mechanism, we compare cases 1 and 2 where only the permeability parameter takes different values. Figure 11a shows decreasing α would significantly destabilizes the flow. This can be explained by substantial increase in the production term. The system is always stable at case 1 ($s_i < 0$) since W_{Re} is always negative and no energy is being transferred to the disturbances. In fact, in this case, the Reynolds stress works against the growth of disturbances. However, once the permeability increases, the production term becomes positive and energy is being transferred to the disturbances. At small and large wavenumbers (i.e., $k < 1.8, k > 3.8$), the system is still stable even though W_{Re} is positive because the dissipation terms overwhelm the production term. However, a range of unstable wavenumbers occurs from $k = 2$ to $k = 4$, where more energy is produced than is dissipated. Note that the viscous energy dissipation D in the fluid layer decreases, while the energy loss G_m due to Darcy drag and viscous dissipation D_m in the porous layer increases at high wavenumbers, i.e. $k \geq 3$. Furthermore, Fig. 11a shows that the decrease of the depth ratio from $\delta = 1$ to $\delta = 0.1$ brings about destabilizing effects on the system. Again, the increase in the production is responsible for the instability. Also, reducing the depth ratio does not have a huge impact on G_m but, it reduces D and intensifies D_m. It was shown in Fig. 7a that imposing the Couette component inserts destabilizing or stabilizing effects depending on the value of permeability parameter α. Here, we consider two porous media: one with high permeability (i.e., $\alpha = 50$) where the Couette component causes an instability in the system and the other one with low permeability (i.e., $\alpha = 500$) where the Couette component enhances the stability. Figure 12a–b displays the neutral curves and variation of growth rate with wavenumber, respectively. For case 1, where $\alpha = 50$, while the energy production due to Reynolds stress and energy loss due to Darcy drag increases considerably for the whole range of wavenumber k as the velocity ratio U^* increases, the change in viscous energy dissipation terms is negligible, see Fig. 12c–f. When $k \leq 3$, the increase in W_{Re} is higher than the increase in G_m; therefore, more energy is being transferred to the disturbances than being dissipated which consequently results in

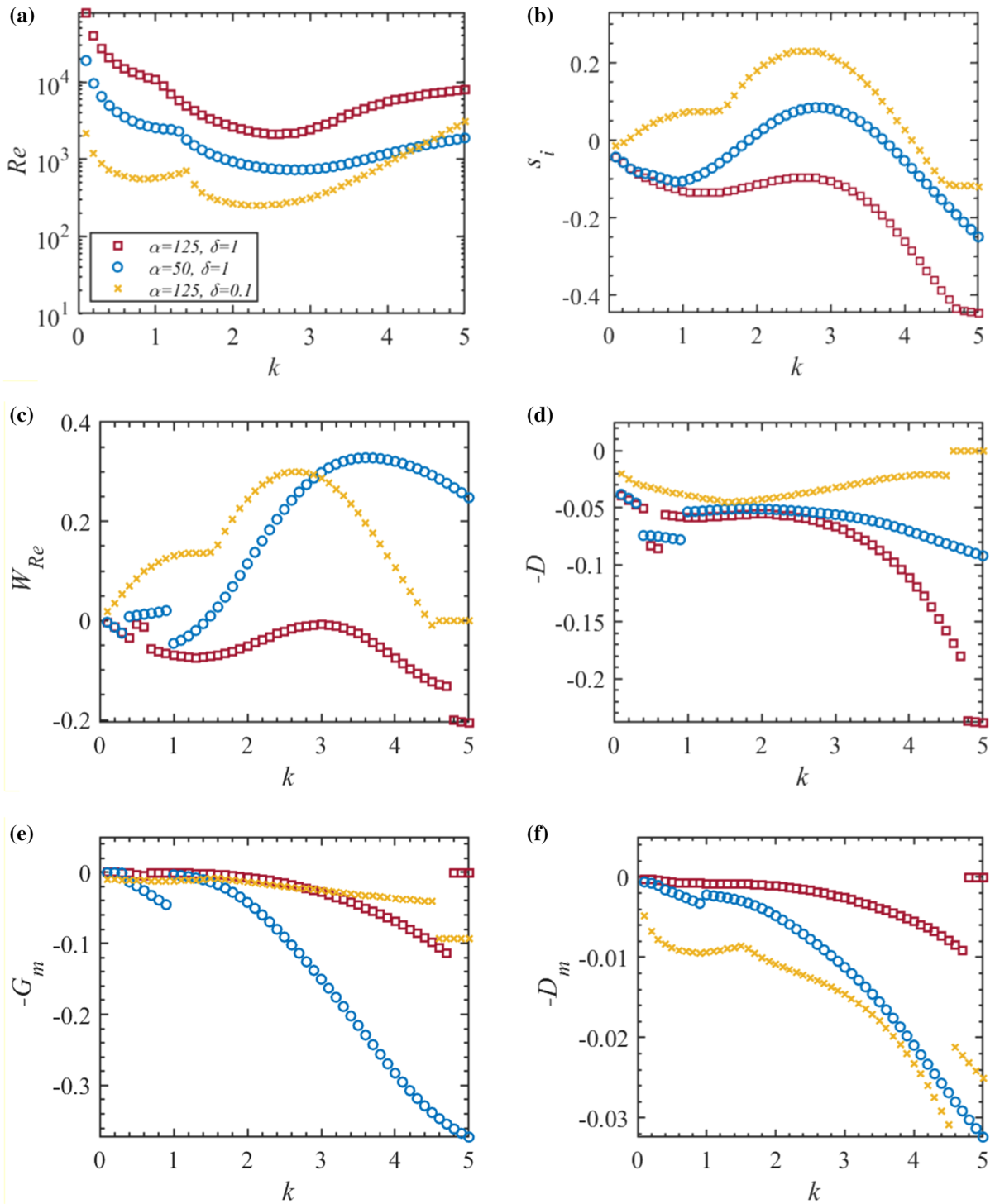

Fig. 11 Variation of **a** Reynolds number, **b** growth rate, **c** Reynolds stress power, **d** viscous energy dissipation in fluid layer, **e** viscous energy loss due to pores, and **f** viscous energy dissipation in porous layer with wavenumber for three different cases. Case 1: $\alpha = 125$, $\delta = 1$, Case 2: $\alpha = 50$, $\delta = 1$, and Case 3: $\alpha = 125$, $\delta = 0.1$. The porosity is $\varepsilon = 0.6$ and $U^* = 0$. Re $= 1000$ for the **b–f**

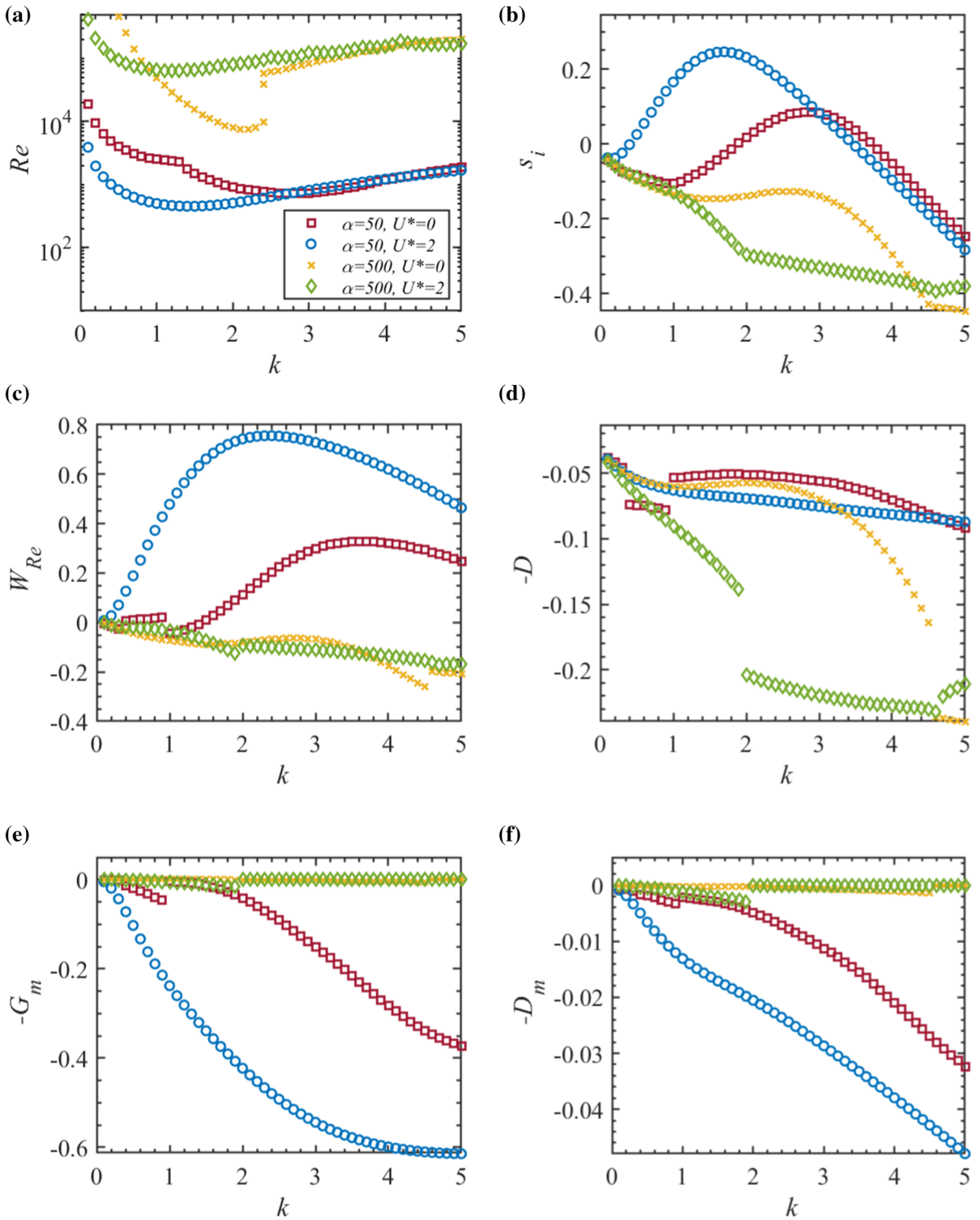

Fig. 12 Variation of **a** Reynolds number, **b** growth rate, **c** Reynolds stress power, **d** viscous energy dissipation in fluid layer, **e** viscous energy loss due to pores, and **f** viscous energy dissipation in porous layer with wavenumber for two different cases with and without the Couette component. Case 1: $\alpha = 50$, and Case 2: $\alpha = 500$. The porosity is $\varepsilon = 0.6$ and $\delta = 1$. Re $= 1000$ for the **b–f**

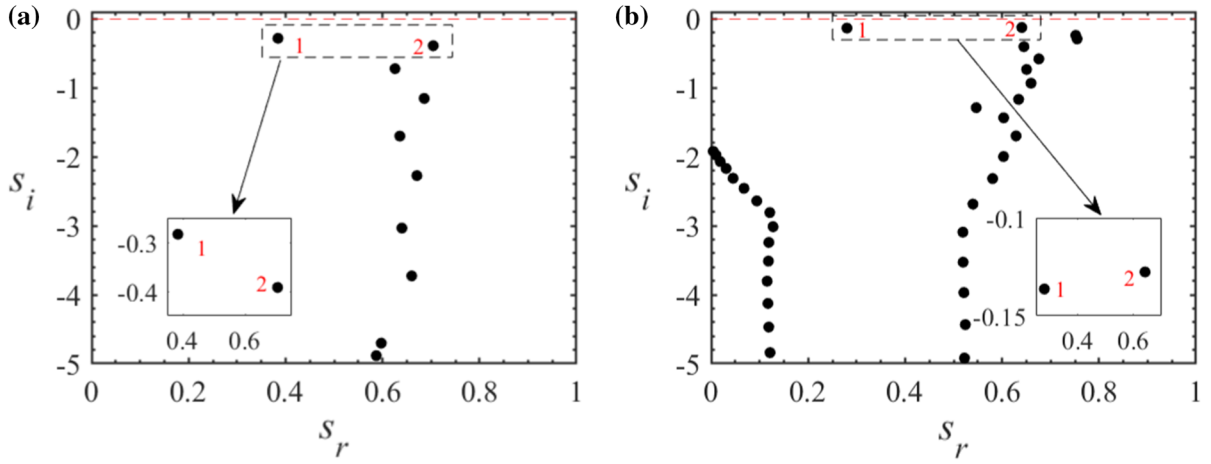

Fig. 13 Eigenvalue spectrum at Re $= 1000$ with $\alpha = 50$ and $U^* = 0$, **a** $k = 0.2$, and **b** $k = 0.8$. The other parameters are $\delta = 1$, and $\varepsilon = 0.6$

an instability in the system. However, as k becomes larger, the change in G_m balances off the increase in W_{Re}. For case 2, where $\alpha = 500$, Fig. 12c, e and f show that the production term and dissipation terms associated to the porous layer are almost invariant with increasing U^*. The only term that is changing is the viscous energy dissipation D in the fluid layer. Since energy dissipation in the fluid layer increases when the Couette component is imposed to the system, the disturbances do not grow and the flow stability enhances. Note that we computed the energy budgets for case 2 at a much higher Reynolds number and we observed that the production term becomes the dominant term.

Interestingly, some of the energy budget curves in Figs. 11 and 12 are discontinuous. For instance, let us consider the case $\alpha = 50$, $\delta = 1$, and $U^* = 0$ in Fig. 12c. It can be seen that a discontinuity occurs in W_{Re}, D, G_m, and D_m profiles when $0.4 \leq k \leq 0.9$. It is suspected that this break is due to mode switching between the leading eigenvalues. To verify this hypothesis, the eigenvalue spectra for $k = 0.2$ and 0.8 are shown plotted and shown in Fig. 13. The two leading eigenvalues are separated by rectangular regions. When $k = 0.2$, the eigenvalue with smaller $s_r = 0.3844$ leads whereas when $k = 0.8$, which is a point on the break, the eigenvalue with higher $s_r = 0.6404$ takes over and dominates the instability, see the blown-up detail. Hence, it is safe to say that the change of leading eigenvalue causes the discontinuities in the energy budget profiles.

6 Conclusion

In this study, we performed a linear stability analysis for a Couette pressure-driven flow in a fluid-layer overlaying porous media. The effect of upper impermeable wall velocity, which generates a Couette flow component, on the stability is discussed in detail with varying the permeability and the thickness of the fluid region. The flow inside the fluid region is governed by the continuity and Navier–Stokes equations, coupled with the flow inside the porous layer governed by continuity and the effective medium approach (i.e., Brinkman equations). The flows in the fluid and porous regions are coupled by the continuity of velocity, normal stress, and tangential stress along the fluid–porous interface proposed by Hill and Straughan [8]. In order to simplify the problem, we only considered porous media with small permeabilities and assumed that the inertial effects are negligible. We validated our results by setting a very large permeability parameter to recover the linear stability of plane PCF flow between two impermeable walls. We found a very good agreement between the present work and the results reported by Potter [16]; in general, adding Couette flow improves the stability when a porous layer is not present.

The results reveal that for a plane Poiseuille flow over a permeable surface, decreasing the permeability or increasing the fluid layer thickness enhances the stability and the flow eventually reaches its most stable state as the porous layer approaches to an impermeable wall. This stabilization has also been observed in previous studies by

Chang et al. [6], Hill and Straughan [8], Tilton and Cortelezzi [10], and Silin et al. [34]. However, once the Couette flow is imposed to the system, the flow becomes more stable or unstable depending on the values of velocity ratio U^*, permeability parameter α and depth ratio δ. It was found that at small α (i.e., large permeability), for example $\alpha = 50$, the Couette component always exerts destabilizing effects while at large values of α it stabilizes the flow. For moderate values of α, for example $\alpha = 100$, the Couette component first destabilizes the flow but as the velocity ratio U^* increases it begins to control the stability and eventually manifest a stabilizing effect. Similar behavior was observed when δ was varied from 0.1 to 5. We called the velocity at which the PCF stability is similar to that of the PF, the cutoff velocity U_{cutoff}. This parameter was first-ever introduced in this study and it was examined as a function of porous permeability and thickness. We found the magnitude of U_{cutoff} drops significantly with increasing α and δ such that for $\alpha \geq 300$ and $\delta \geq 0.8$ the stability of the system will be enhanced by imposing Couette components in the $10^{-2} \sim 10^{-1}$ order of magnitude. The significance of cutoff velocity can be exploited in accordance with the relevant applications involving flows over porous materials. In applications such as mixing, it is desired to create an instability to enhance the process efficiency which could be achieved by imposing a Couette component less than U_{cutoff}. However, in other applications including food processing or pharmaceutical industries the goal is to avoid chaotic flows by keeping the system stable and this can be carried out by imposing a Couette component greater than U_{cutoff}. Therefore, being able to accurately predict the flow behavior in the presence of Couette component is crucial where this study provides a deeper understanding of such behavior.

Finally, to decipher the physics behind the impacts of imposing Couette flow with the existence of a porous surface on the stability, we performed the energy budget analysis. The results show that for a Poiseuille flow over a porous surface, when the permeability or the fluid layer thickness increases, the power of Reynolds stress against the base flow shear increases significantly. Since this production term is responsible for transferring energy to the disturbances, more energy is being transferred to the flow; consequently, makes the system less stable. In the presence of Couette flow, the energy production term is responsible for the instability at small α such as $\alpha = 50$. However, at higher α values, for example $\alpha = 500$, imposing Couette flow increases the energy dissipation in the fluid layer; hence, more energy is being dissipated than being transferred leading to enhance the stability.

The results presented in this study will provide a step forward in understanding and analyzing the behavior of a plane Newtonian Poiseuille–Couette flow over a permeable surface. These results have the potential to be used as a first step towards examining the behavior of pressure-driven complex flows over permeable surfaces that are encountered in different applications including mirco-, bio-devices. Further experiments are desired to validate the current results that are the subject of our current investigation.

Acknowledgements This research was supported by the Army Research Office (ARO) under Award No. W911NF-18-1-0356 to S.M. and P.M.

Appendix A

In order to check the convergence of spectrum obtained from the numerical experiment, the relative error is defined as mentioned in Tilton and Cortelezzi [10].

$$e_N = \frac{\|c_{N+1} - c_N\|_2}{\|c_N\|_2}, \tag{A.1}$$

where $\|\bullet\|$ represent the L_2 norm. c_{N+1} and c_N are vectors whose components are the least twenty stable eigenvalues calculated using $N + 1$ and N, respectively, in each region. Figure 14 illustrates the variation of error function with respect to the number of collocation points N. It can be seen that for both cases $U^* = 0$ & 1, roughly 75 Chebyshev polynomials is required to attain an error on the order of 10^{-6}. Hence, we performed our calculations using 75 Chebyshev polynomials.

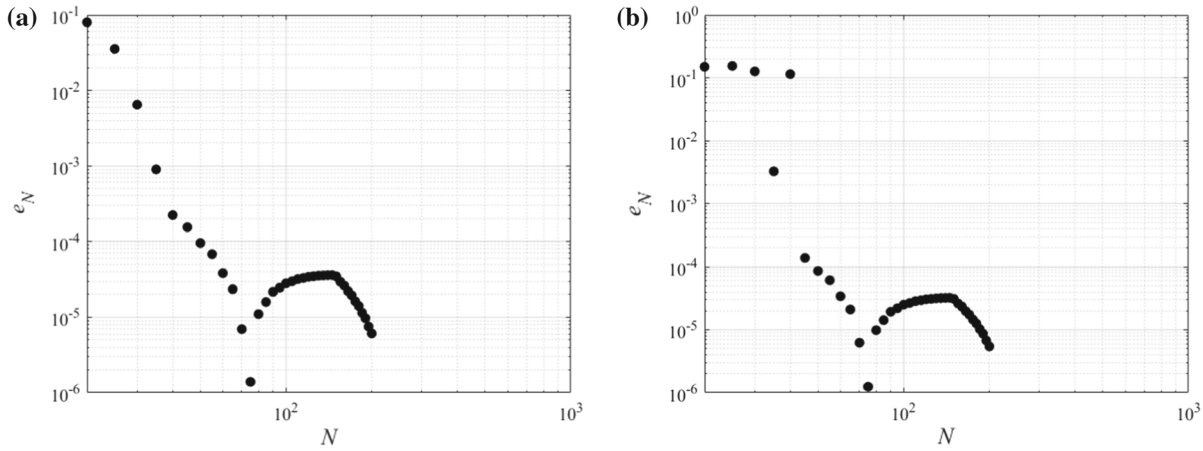

Fig. 14 Log–log plot of the variation of the relative error, e_N, with the number of Chebyshev polynomials, N, employed to solve the eigenvalue problem for the case $k = 1$, Re $= 1000$, $\alpha = 75$, $\delta = 1$, $\varepsilon = 0.6$, (a) $U^* = 0$, and (b) $U^* = 1$

References

1. Bickerton S, Govignon Q, Kelly P (2013) Resin infusion/liquid composite moulding (LCM) of advanced fibre-reinforced polymer (FRP). Advanced fibre-reinforced polymer (FRP) composites for structural applications. Elsevier, Amsterdam, pp 155–186
2. Perazzo A, Tomaiuolo G, Preziosi V, Guido S (2018) Emulsions in porous media: From single droplet behavior to applications for oil recovery. Adv Colloid Interface Sci 256:305–325
3. Breugem WP, Boersma BJ, Uittenbogaard RE (2006) The influence of wall permeability on turbulent channel flow. J Fluid Mech 562:35–72
4. Sohel Murshed SM, Nieto de Castro CA (2017) A critical review of traditional and emerging techniques and fluids for electronics cooling. Renew Sustain Energy Rev 78:821–833
5. Samanta A (2020) Linear stability of a plane Couette–Poiseuille flow overlying a porous layer. Int J Multiphase Flow 123:103160
6. Chang M-H, Chen F, Straughan B (2006) Instability of Poiseuille flow in a fluid overlying a porous layer. J Fluid Mech 564:287–303
7. Beavers GS, Joseph DD (1967) Boundary conditions at a naturally permeable wall. J Fluid Mech 30:197–207
8. Hill AA, Straughan B (2008) Poiseuille flow in a fluid overlying a porous medium. J Fluid Mech 603:137–149
9. Liu R, Liu QS, Zhao SC (2008) Instability of plane Poiseuille flow in a fluid–porous system. Phys Fluids 20:104105
10. Tilton N, Cortelezzi L (2008) Linear stability analysis of pressure-driven flows in channels with porous walls. J Fluid Mech 604:411–445
11. Wu Z, Mirbod P (2019) Instability analysis of the flow between two parallel plates where the bottom one coated with porous media. Adv Water Resour 130:221–228
12. Ghosh S, Usha R, Sahu KC (2014) Linear stability analysis of miscible two-fluid flow in a channel with velocity slip at the walls. Phys Fluids 26(1):014107
13. Chattopadhyay G, Sahu KC, Usha R (2019) Spatio-temporal instability of two superposed fluids in a channel with boundary slip. Int J Multiph Flow 113:264–278
14. Chattopadhyay G, Usha R, Sahu KC (2017) Core-annular miscible two-fluid flow in a slippery pipe: A stability analysis. Phys Fluids 29:097106
15. Chattopadhyay G, Ranganathan U, Millet S (2019) Instabilities in viscosity-stratified two-fluid channel flow over an anisotropic-inhomogeneous porous bottom. Phys Fluids 31(1):012103
16. Potter MC (1966) Stability of plane Couette–Poiseuille flow. J Fluid Mech 24:609–619
17. Reynolds (1967) WC & Potter, MC. J Fluid Mech 1967(27):465
18. Hains FD (1967) Stability of Plane Couette–Poiseuille Flow. Phys Fluids 24(3):609–619
19. Thomas LH (1953) The stability of plane Poiseuille flow. Phys Rev 91:780–783
20. Cowley S, Smith F (1985) On the stability of Poiseuille–Couette flow: a bifurcation from infinity. J Fluid Mech 156:83–100
21. Guha A, Frigaard IA (2010) On the stability of plane Couette–Poiseuille flow with uniform cross-flow. arXiv:1003.3247
22. Chang T-Y, Chen F, Chang M-H (2017) Stability of plane Poiseuille–Couette flow in a fluid layer overlying a porous layer. J Fluid Mech 826:376–395
23. Ochoa-Tapia JA, Whitaker S (1995) Momentum transfer at the boundary between a porous medium and a homogeneous fluid–II. Comparison with experiment. Int J Heat Mass Transf 38:2647–2655
24. Ochoa-Tapia JA, Whitaker S (1995) Momentum transfer at the boundary between a porous medium and a homogeneous fluid–I. Theoretical development. Int J Heat Mass Transf 38:2635–2646

25. Mirbod P, Andreopoulos Y, Weinbaum S (2009) Application of soft porous materials to a high-speed train track. J Porous Media 12:11
26. Whitaker S (1986) Flow in porous media I: A theoretical derivation of Darcy's law. Transp Porous Media 1:3–25
27. Dolapçi İ (2004) Chebyshev collocation method for solving linear differential equations. Math Comput Appl 9:107–115
28. Makinde OD (2009) On the Chebyshev collocation spectral approach to stability of fluid flow in a porous medium. Int J Numer Meth Fluids 59:791–799
29. Drazin PG, Reid WH (2004) Hydrodynamic stability. Cambridge University Press, Cambridge
30. Worster MG (1992) Instabilities of the liquid and mushy regions during solidification of alloys. J Fluid Mech 237:649–669
31. Lin S (1970) Roles of surface tension and Reynolds stresses on the finite amplitude stability of a parallel flow with a free surface. J Fluid Mech 40:307–314
32. Kelly R, Goussis D, Lin S, Hsu F (1989) The mechanism for surface wave instability in film flow down an inclined plane. Phys Fluids A 1:819–828
33. Ghosh S, Loiseau J-C, Breugem W-P, Brandt L (2019) Modal and non-modal linear stability of Poiseuille flow through a channel with a porous substrate. Eur J Mech B Fluids 75:29–43
34. Silin N, Converti J, Dalponte D, Clausse A (2011) Flow instabilities between two parallel planes semi-obstructed by an easily penetrable porous medium. J Fluid Mech 689:417–433